1 SUPPLEMENTARY INFORMATION: Velocity Map Images from Surface-Hopping, Reactive Scattering Trajectories of OH (Σ) + H_2.

Christopher Robertson
Martin J. Paterson
email: m.j.paterson@hw.ac.uk
School of Engineering & Physical Sciences. Heriot-Watt University, Edinburgh, Scotland UK EH14 4AS

2 Numerical Details

The Wigner distribuition is obtained from the ground, pure (no temperature) state solution of the 1D potential (at far distances), the distribuition integral is performed numerically and sampled using Monte-Carlo. We chose the default parameters in SHARC kinetic energy correction by rescaling of the parallel components of the nuclear velocity vector. The velocity vector is not modified upon frustrated hops. Decoherence schemes have also been applied to previous simulations of this system. We used the energy-based decoherence as described by Granucci *et al*, with energy parameter of 0.1 as the suggested default value in SHARC. The same orientations and impact parameters where used for both models, but the Wigner distribuition depended on the model PES. The regular lattice used for the impact parameter coordinate determined the cross-section weight each trajectory has. The cross section was approximated as follows:

$$\sigma_{coll} = 2\pi \sum_{k=0}^{N^b+1} \int_{b_k}^{b_{k+1}} bdbP(b) \approx 2\pi \sum_{k=0}^{N^b+1} P(b_{\bar{k}})[b_{k+1}^2 - b_k^2] \tag{1}$$

Where we partitioned the impact parameter domain into N^b bins, the summation runs over the edges of each bin, and $b_{\bar{k}}$ corresponds to the midpoint of the k'th bin. Where $P(b)$ is the density, which itself can be broken into distinct j channels:

$$P(b_{\bar{k}}) = \sum_j P_j(b_{\bar{k}}) \approx \sum_j \frac{n_{jk}}{N_k}(b_{\bar{k}}) \tag{2}$$

Where n_{jk} is the number of trajectories in the k'th impact parameter bin for the j'th channel, the sum of all channels is N_k.

3 VMI: Ortiz-Suárez, Mariví and Witinski, Mark F. and Davis, H. Floyd, JCP, 20, 124, 2006

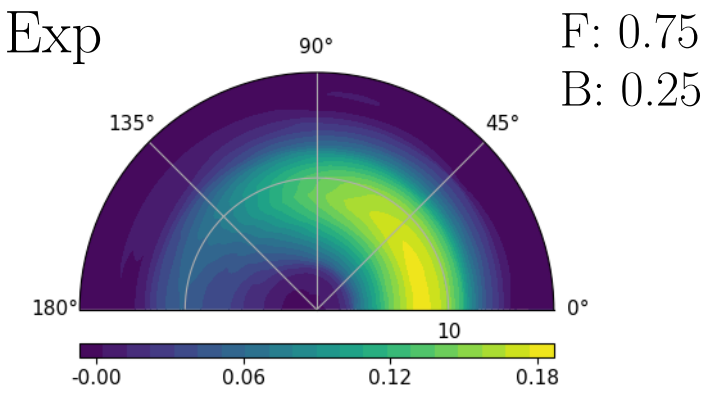

Figure 1: VMI from Ortiz-Suárez, Mariví and Witinski, Mark F. and Davis, H. Floyd, JCP, 20, 124, 2006

4 Greater or less than $b = 3\mathring{A}$ VMI

We employed the Uniform phase-space binning procedure for both velocities and angles as described by references 20 and 21 of the article. (R. Bernstein, Atom-molecule collision theory (Chp. 16), Plenum P., N. York, 1979. and M. B. Faist, The J.Chem.Phys., 1976, 65, 5427–5435).

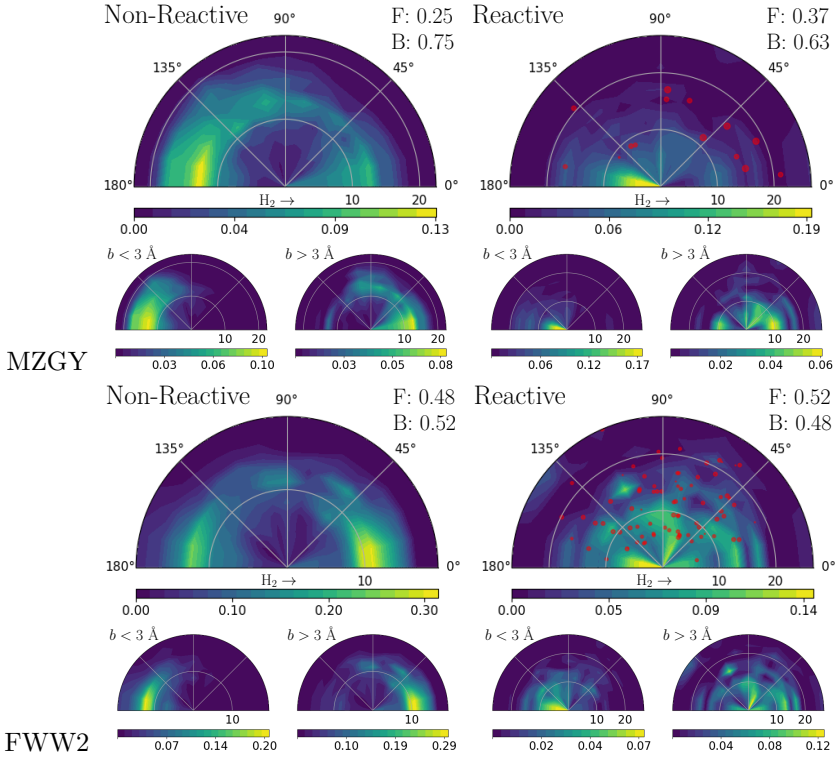

Figure 2: Velocity Map images of the quenched H_2 (*left*) or H product (*right*) from the reactive quenching channel in the MZGY (*upper*) and FWW2 (*lower*) models. The smaller pair of cells correspond the VMI for impact parameters b greater or less than 3 Å. The "F" and "B" labels describe the cross section fraction in the "Forward" ($< \pi/2$) or "Backward" ($> \pi/2$) directions. The red scattered points in the plot show the OH nascent H atoms, with a size proportional to their cross-section weight.

5 PES and Derivative Couplings of FWW2 and MZGY

Potential energy (bottom cells) and derivative couplings (top cells) for both models (left FWW2, right MZGY) between the intermolecular distance and some other polar angle indicated in the title figure and caption. Derivative coupling: the values shown are the norm of the vector, averaged over a 5 point grid ($\pm$ 0.2,$\pm$0.1,0.0) for both H_2 and OH stretches. If the state energies exceed 5.0 eV ($\approx$4.0 eV is the S_2 far apart minima) that sample is disregarded from the average, since it is unlikely to be accessed under any initial conditions (particularly when sampling the Wigner OH/H_2 vibrational distribution).
Both plots show the PES and coupling strengths to be qualitatively similar. The only exception is the derivative coupling peak at $\approx 140^\circ$ present and dominant in the top cell of Figure 3, which corresponds to a preference of H facing OH quenching which is notably absent in MGYZ. This difference may go some way to explain the differences between models.

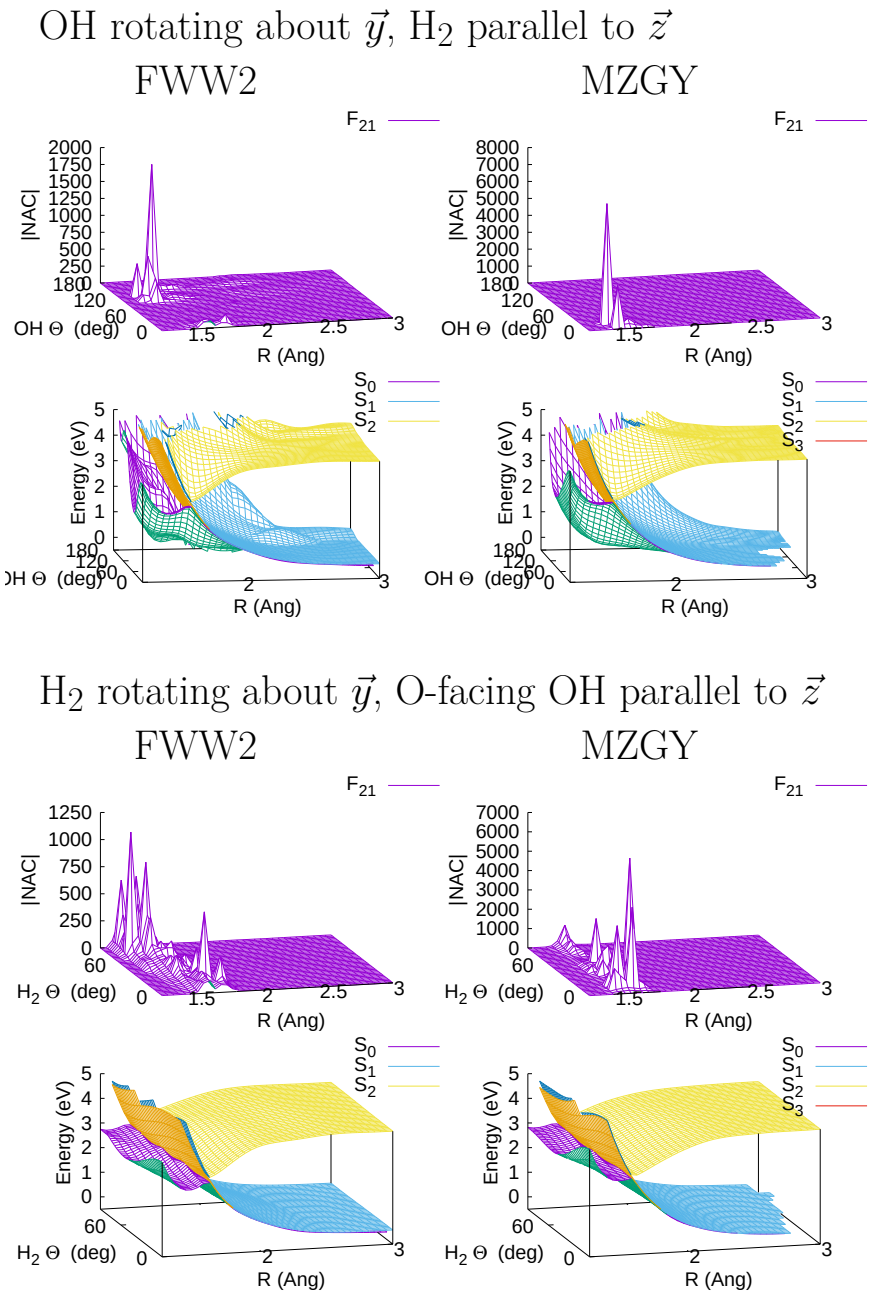

Figure 3: TOP, θ_{OH} - 180° corresponds to H facing OH; BOTTOM, θ_{H_2} - 90° corresponds to H_2 perpendicular to a O facing OH (at 0 °).

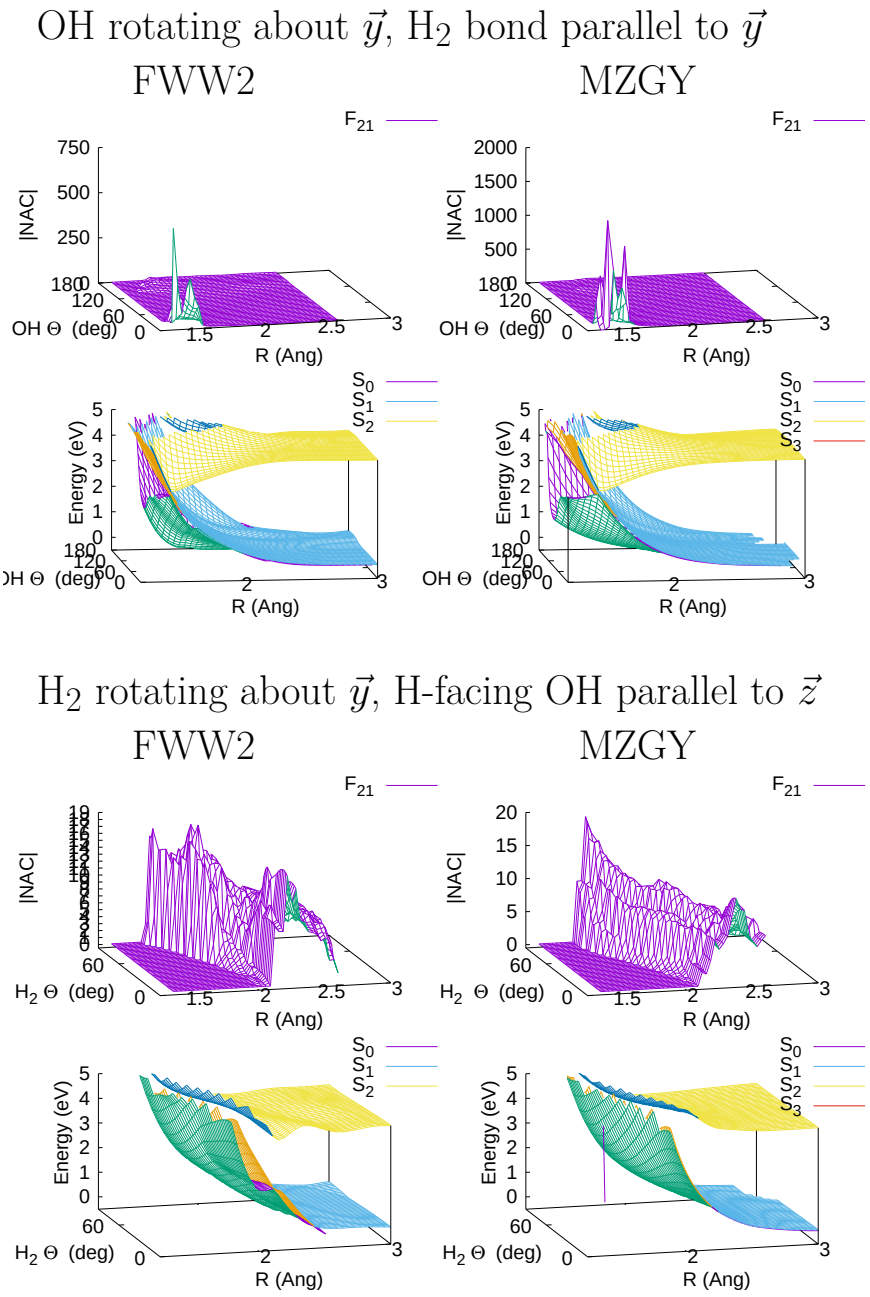

Figure 4: TOP, θ_{OH} - 180° corresponds to H facing OH (out of plane rotation); BOTTOM, θ_{H_2} - 90° corresponds to H_2 perpendicular to a H facing OH (at 180 °).

6 Hopping Event geometries

Figure 5 shows that, as noted in the article, for FWW1 hopping occurs largely at H facing OH geometries with only a comparatively minor channel with O facing OH, where MZGY shows the same channels but with the opposite emphasis.

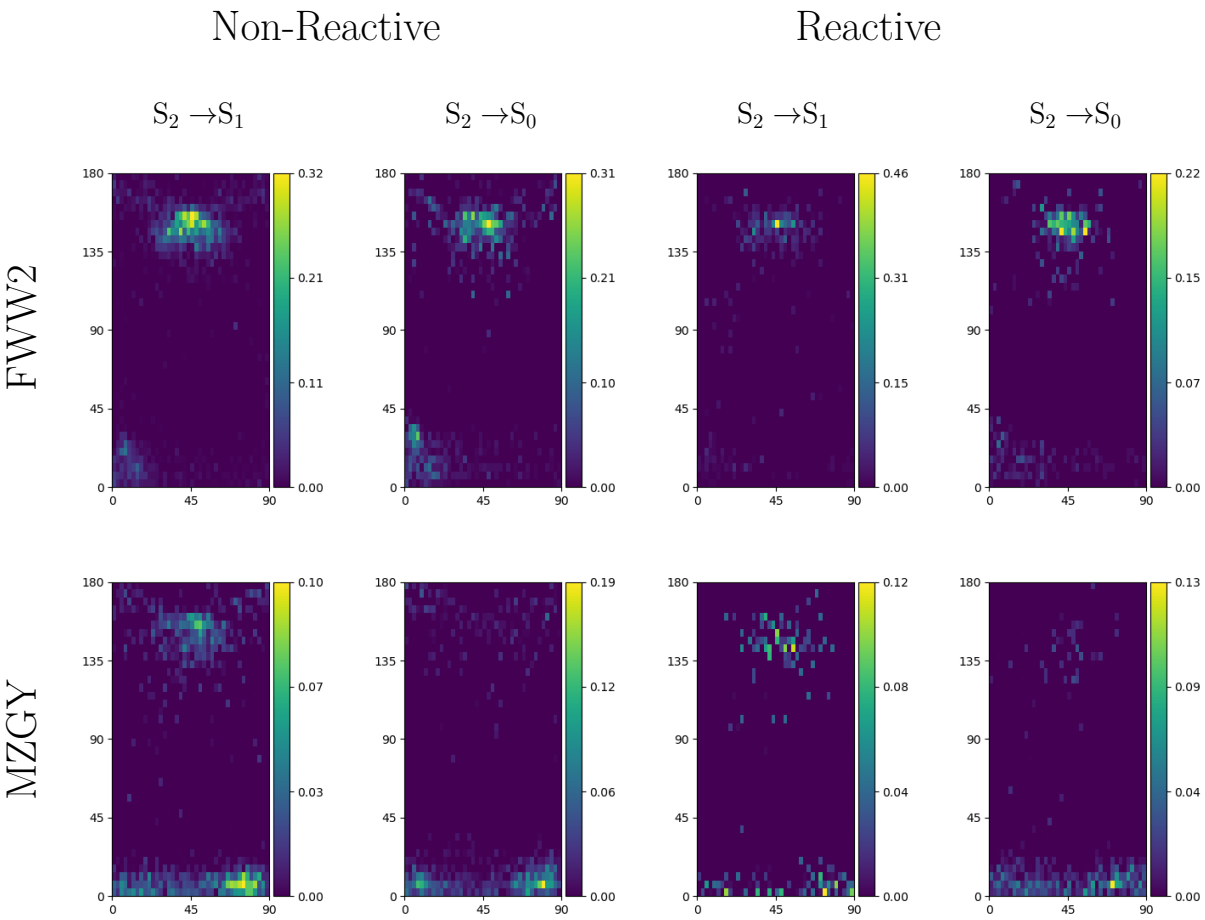

Figure 5: Histogram of $S_2 \rightarrow S_1$ and $S_2 \rightarrow S_0$ surface hopping events weighted by cross section as a function of $\theta_{OH} = acos(\vec{R} \cdot \vec{r_{OH}}/|Rr_{OH}|)$ (0-180°) and θ_{H_2} (0-90°). 180 θ_{OH} corresponds to H facing OH.

7 Coupling strengths at Hopping geometries.

Figure **??** shows the mean norm of the non-adiabatic coupling vector as a function of the OH H2 intermolecular angle (as defined for Figure 2 in the article) for the hopping event geometries. For MZGY the $S_2 \rightarrow S_1$ reactive (Rx) and non reactive (NR) have similar distributions, and similar in $S_2 \rightarrow S_0$. For O-facing OH (acute) angles we see slightly higher values, in particular for Reactive channels. The dip around 110° coincides with the longer lifetimes seen in Figure 7, which FWW2 is similar, but $S_2 \rightarrow S_0$ have a larger norm for acute angles (O facing OH), while $S_2 \rightarrow S_1$ is larger at obtuse angles. Overall the strength of the derivative coupling cannot be the reason for FWW2 observed preference for the H-facing OH reactive channel. A better explanation is offered by the following section.

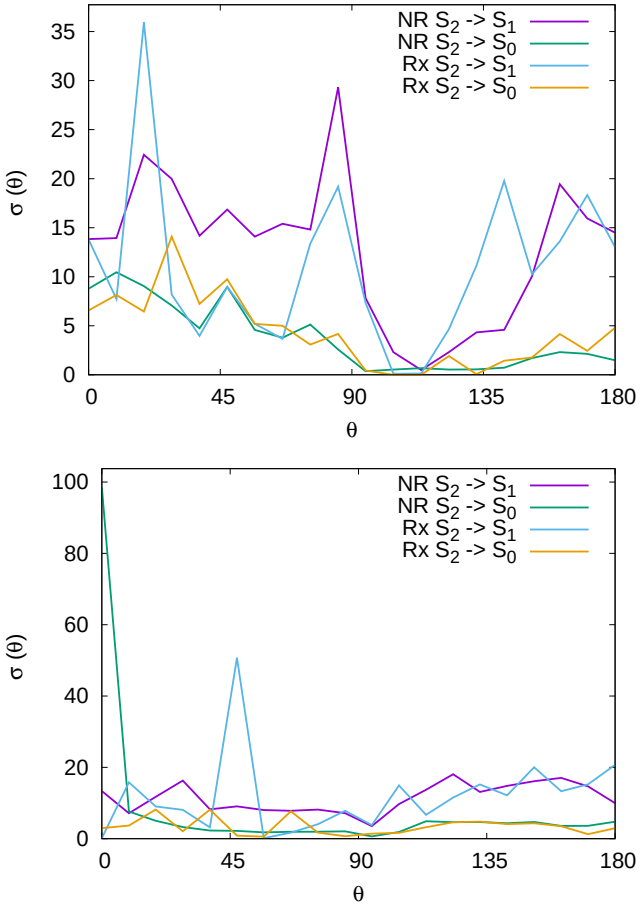

Figure 6:

8 OH_3 complex lifetimes

Figure 7 shows the average OH–H_2 complex lifetime of the quenched trajectories as a function of the angle θ; this angle is between the OH and H 2 bond vectors. The H_2 vector is defined as always pointing away from the Oxygen. Zero degrees corresponds to the OH Oxygen facing the incoming H_2 , while 180 to OH Hydrogen facing the incoming H_2 The most salient feature for this article concerns the difference in the reactive trajectories between the FWW2 and MZGY models; FWW2 exhibits nearly three times as long lifetime at H facing OH angles than at O facing OH. In contrast, MZGY appears to have little preference over which angle.

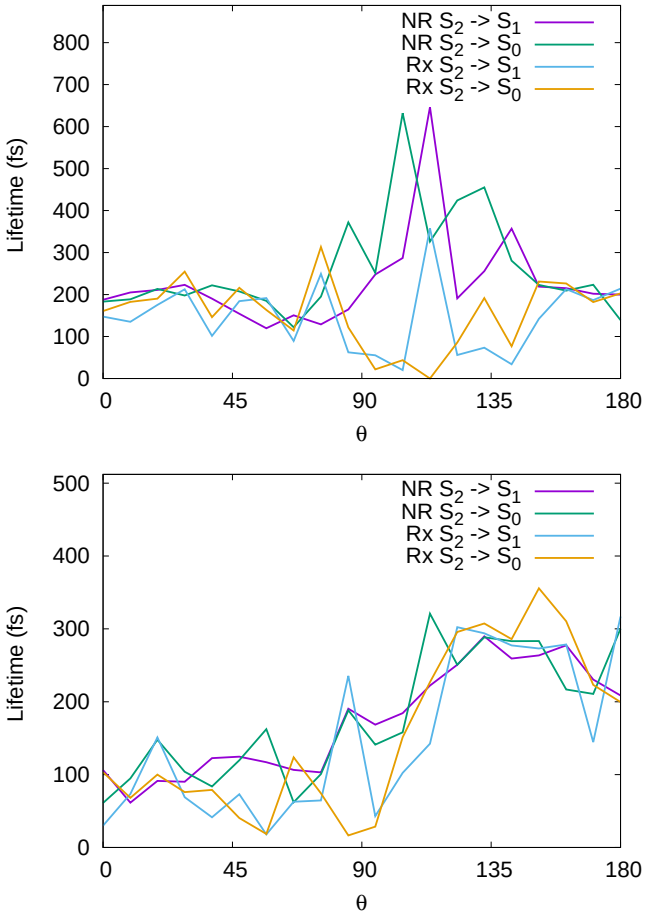

Figure 7: The average lifetime of the OH–H_2 interacting Complex as a function of θ. Its defined as the time between OH/H 2 intermolecular incoming distance of 2.5 Å and outgoing distance 4.0 Å as cutoffs. MGZY (*top*) FWW2 (*bottom*)

9 Rovibrational spectra

At sufficient intermolecular distances (> 6 Å) the H_2 and OH stretch PES become decoupled. A Morse model is fitted to the PES and used to estimate, together with the velocity (parallel to the bond vector) of the outgoing diatom, the internal energy E_I, which is averaged over a few oscillations. The eigenvalues of the Morse Hamiltonian are analytically known and the vibrational state is identified as the nearest in energy to E_I. The remaining rotational energy (perpendicular to the bond vector velocity) E_R is easily calculated and the non-rigid rotor Hamiltonian parameters can also be obtained from a Morse oscillator model, as well as the non-rigid rotor eigenstates; the rotational state is identified as the nearest in energy to E_R.

10 FWW2 Rovibronic Spectra

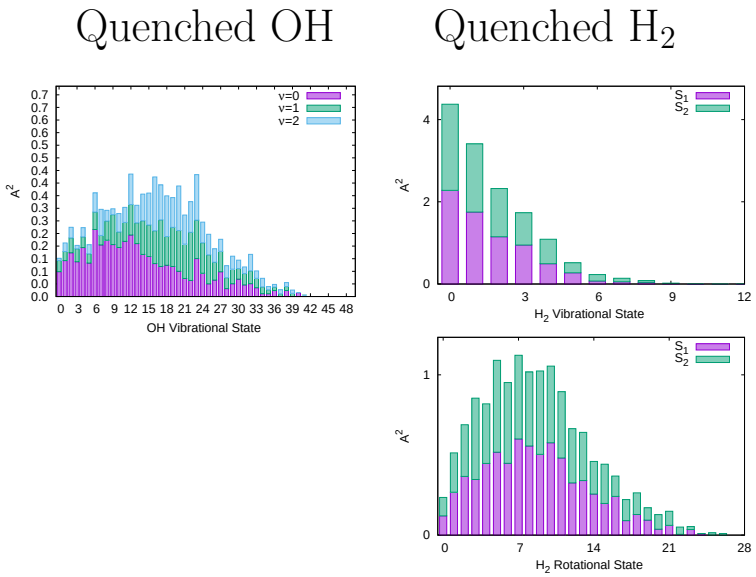

Figure 8: Left rovibronic spectra. Right - vibrational, rotational spectra

11 MZGY Rovibronic Spectra

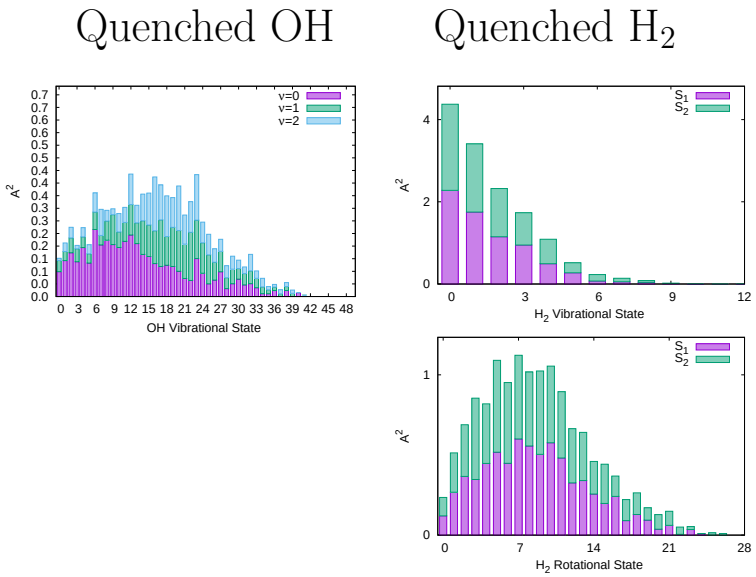

Figure 9: Left rovibronic spectra. Right - vibrational, rotational spectra

12 FWW1 PES

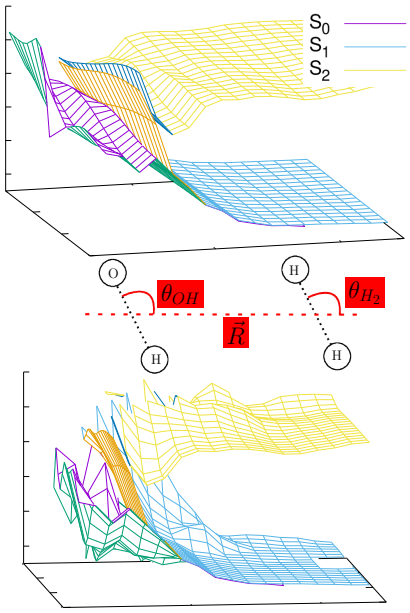

Figure 10: Potential energy surfaces along two coordinates, the intermolecular distance $\vec{R}$ and the $\theta_{\mathrm{H_2}}$ (θ_{OH}) angle between $\vec{R}$ and the H_2 (OH) internal coordinate *top* (*bottom*), keeping other coordinates at zero. This is the FWW1 model

13 FWW1 VMI

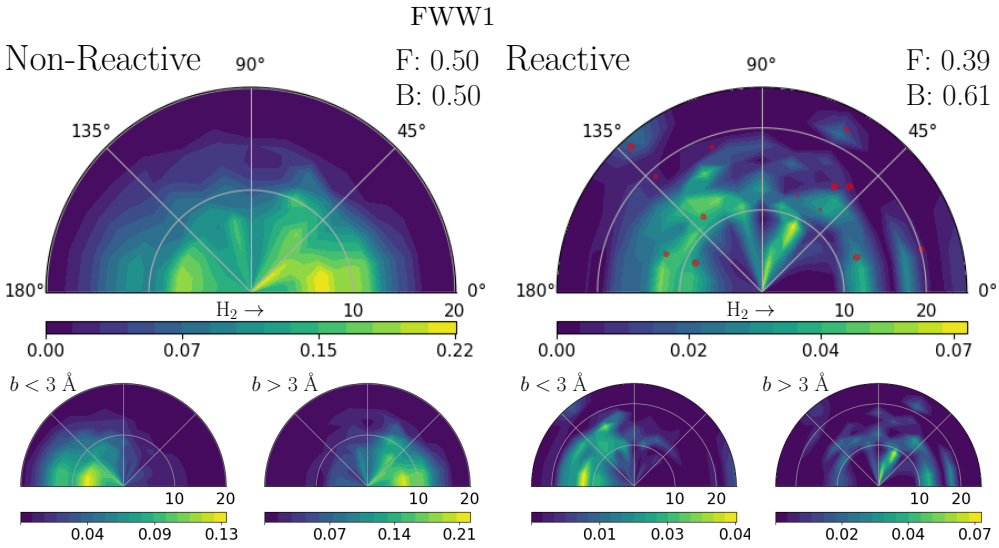

Figure 11: Velocity Map images of the quenched H_2 (*left*) or H product (*right*) from the reactive quenching channel FWW1 model. The smaller pair of cells correspond the VMI for impact parameters b greater or less than 3 Å. The "F" and "B" labels describe the cross section fraction in the "Forward" ($< \pi/2$) or "Backward" ($> \pi/2$) directions. The red scattered points in the plot show the OH nascent H atoms, with a size proportional to their cross-section weight.

14 FWW1 ANGLE DIFF CROSS SECTION

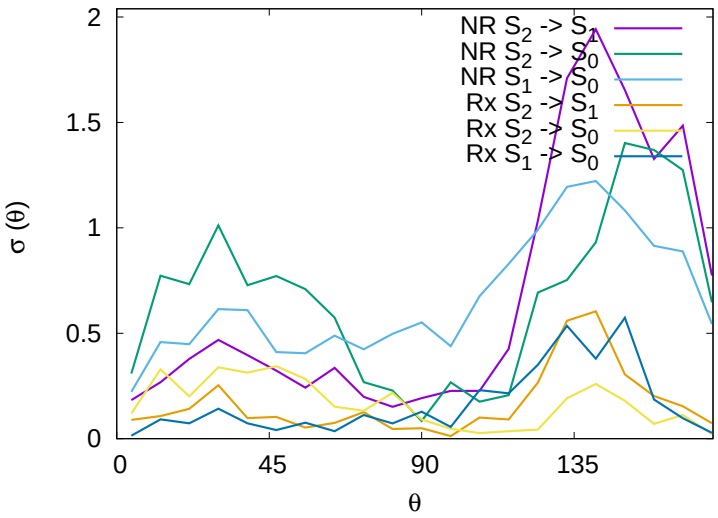

Figure 12: Differential cross section as a function of the angle between the OH and H_2 bond vectors as described in text, at the first instance of quenching for 6 different channels: Non Reactive (NR) from $S_2 \rightarrow S_1$ (purple), $S_2 \rightarrow S_0$ (green), $S_1 \rightarrow S_0$ (light-blue); Non reactive (NR) from $S_2 \rightarrow S_1$ (orange), $S_2 \rightarrow S_0$ (yellow), $S_1 \rightarrow S_0$ (dark-blue)

15 FWW1 CHANNEL CROSS SECTION

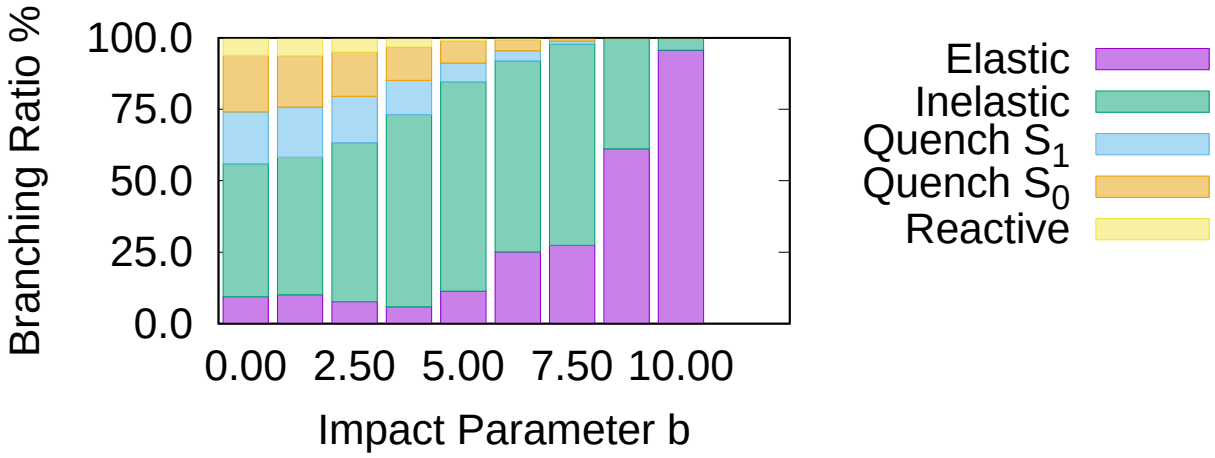

Figure 13: Branching rations for the different channels as a function of impact parameter, models FWW1 (*top*).

16 FWW1 H KE DISTRIBUITION

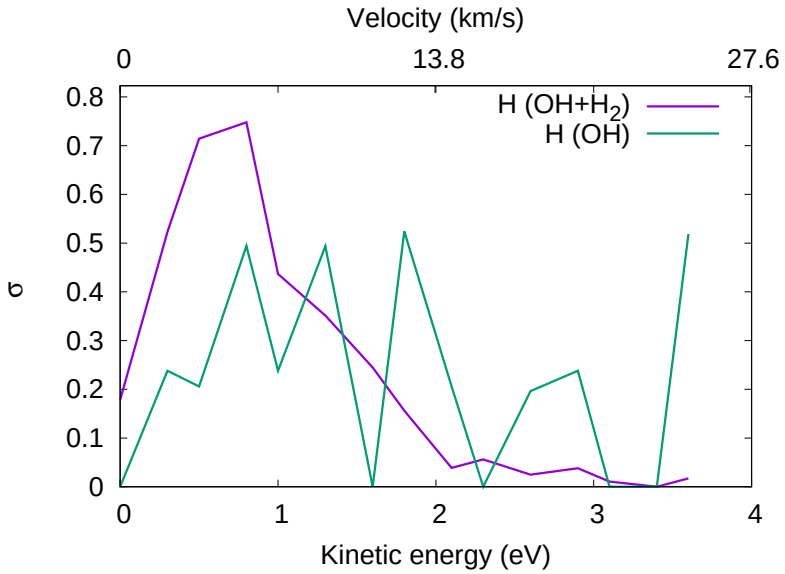

Figure 14: H product kinetic energy distribution in the FWW1 model. The OH nascent H product are shown also in green (x10).

17 FWW1 ROVIBRAONIC SPECTRA

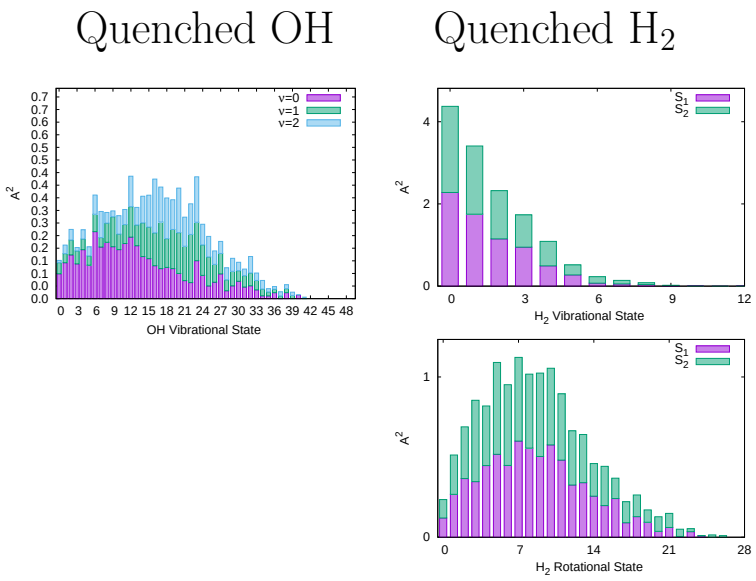

Figure 15: Left rovibronic spectra. Right - vibrational, rotational spectra